PCCP

Accepted Manuscript

This is an *Accepted Manuscript*, which has been through the Royal Society of Chemistry peer review process and has been accepted for publication.

Accepted Manuscripts are published online shortly after acceptance, before technical editing, formatting and proof reading. Using this free service, authors can make their results available to the community, in citable form, before we publish the edited article. We will replace this *Accepted Manuscript* with the edited and formatted *Advance Article* as soon as it is available.

You can find more information about *Accepted Manuscripts* in the Information for Authors.

ROYAL SOCIETY OF CHEMISTRY

www.rsc.org/pccp

Journal Name

ARTICLE TYPE

Nanoscale interface engineering in ZnO twin nanorods for proposed phonon tunnel devices

Avanendra Singh[1], Kartik Senapati[1*], Biswarup Satpati[2], Mohit Kumar[3], and Pratap K. Sahoo[1]*

Zinc oxide twin nanorods, with two identical crystalline sections connected by an amorphous layer, were reproducibly grown by a simple one-step hydrothermal technique. The thickness of the amorphous layer between the crystalline segments was tunable with growth parameters, as confirmed by high resolution transmission electron microscopy. The photoluminescence spectra of these twin nanorods exhibit strong near band edge emission in the UV range, with convoluted phonon sidebands. De-convolution analysis of these spectra showed that the amorphous inter layers act as effective phonon barrier beyond certain thickness. Such oriented grown individual crystalline-amorphous-crystalline structures may be a suitable test system for fundamental studies of phonon tunneling in nanostructure. While physical vapor deposition techniques are seriously constrained in realizing crystalline-amorphous-crystalline structures, our results show the viability of engineering embedded interfaces by chemical routes.

Introduction:

Fundamental understanding of the phonon transport process in nanostructures is rapidly gaining importance[1-3] because phonons can both be detrimental and beneficial to the functionality of nanoscale devices. For example, optoelectronic applications of widely studied ZnO based devices[4-8] invariably excite optical phonon modes in the system due to the built-in polarity in the crystal structure[9]. From the perspective of electronic transport in these devices, minimization of electron-phonon scattering is desirable, whereas, efficient phonon transport is essential from the perspective of waste heat management in the nano-structures for large scale integration. Therefore, optimization of phonon transport is an important design consideration for the present day nanoscale devices. In this context, understanding phonon tunneling process assumes analogous importance as understanding electron tunneling in nano-junctions. There are, however, little experimental efforts towards a direct study of phonon tunneling in mesoscopic structures. Recently, Cole *et al.*[10] analyzed the clamping loss in micro-mechanical resonators using a phonon tunneling approached developed by Wilson-Rae[11]. However, a junction based phonon-tunneling measurement, truly analogous to metal-insulator-metal type electron tunnel junctions, is still lacking in the literature. The insulating barrier between the metallic electrodes, in an electron tunnel junction, forbids classical electron transport across the junction. However, when the insulating barrier is made sufficiently thin, quantum mechanics allows for a finite probability of electron tunneling across the junction. In the same spirit, a phonon junction should ideally comprise of a thin amorphous layer sandwiched between two crystalline segments grown with the same crystal orientation. Since the amorphous layer can damp out certain phonon modes which freely propagate through the crystalline segments, such crystalline-amorphous-crystalline (CAC) structures can facilitate a true phonon tunneling measurement. A major obstacle for such measurements is the difficulty in fabricating CAC structures with tunable barrier thickness. Typically, electron tunnel junctions are prepared by a combination of lithographic techniques and in-situ physical vapor deposition of metals and insulator layers. For an equivalent phonon tunnel junction, one ideally requires a CAC structure where both crystalline segments have the same lattice orientation. In the standard physical vapor deposition techniques, such as sputtering, evaporation, and pulsed laser deposition etc., it is almost impossible to grow an oriented structure on top of an amorphous layer. Here we overcome this difficulty by employing

the well established aqueous solution based chemical growth techniques of oriented semiconducting nanorods. ZnO is ideally suited for this purpose due to the well established growth techniques and due to the polar nature of ZnO crystal, which excites optical phonon modes.

Due to the large exciton binding energy and wide band gap, ZnO has been extensively studied in the literature[12,13] as potential optoelectronics material[5-8], energy material[14-15], and sensing applications[16]. Typically free standing aggregates of ZnO nanostructures are prepared for these studies, using vapor phase[17,18] or aqueous solution based[19-21] growth methods. Among the standard processing routes of ZnO, hydrothermal method[22-24] is a particularly simple, low temperature (≤ 90 ^{0}C) route which provides multiple control parameters such as, temperature, pressure, molarity of the aqueous solution, and choice of precursors. A variety of multiply connected low dimensional ZnO structures have also been reported in the literature[25-30] prepared by the hydrothermal route[27-30]. Recently, the growth of twin Nanosphere and nanorods have generated considerable interest due to their unique anisotropic light emission[31-33]. In this paper we report controllable growth of CAC type ZnO nanorods using the simple hydrothermal route. A closer inspection of the segmented nanorods by transmission electron microscopy confirmed two identical segments of single crystalline ZnO connected through a well defined amorphous interface. Since the width of these amorphous barriers was controllable via growth parameters, such twin-nanorod junctions (TNRJs) are suitable candidates for a systematic study of phonon tunneling process. We discuss the suitability of these TNRJs for phonon tunneling experiments based on the analysis of photo-luminescent (PL) spectra.

Experimental details

P-type Si (100) substrates were used in all case. Prior to nanowire growth, all substrates were coated with a thin layer of ZnO (~30 nm) using pulsed DC magnetron sputtering in a vacuum chamber with a base pressure of 2×10^{-7} mbar. The sole purpose of the ZnO coating was to ensure a fixed surface chemistry for all samples. Twin ZnO nanorods were synthesized by hydrothermal process using GR grade Zinc nitrate hexahydrate (Zn(NO$_3$)$_2$. 6H$_2$O, 99%) and hexamethylenetetramine (HMTA, (CH$_2$)$_6$N$_4$, 99.99%),

from Sigma-Aldrich. An aqueous solution mixture of both Zinc nitrate and HMTA was prepared in 1:1 ratio with three different molar concentration of 0.01, 0.05 and 0.1 M by continuously stirring on a stir plate for 30 minutes. A screw capped laboratory 30 ml Borosil bottle was filled with the mixture placing the ZnO coated substrates under the cap with the surface facing down in to the reaction precursor. The nanorod growth was initiated by placing the bottle in a water bath on a regular laboratory oven. Samples were prepared at reaction temperatures ranging from 60 ^{0}C to 90 ^{0}C. In order to vary the growth duration, keeping all other parameters same, we placed separate identical screw capped bottles simultaneously in the water bath. The temperature of the reaction mixture was raised to the desired reaction temperature in 30 minutes in all cases, starting from room temperature of ~ 30 ^{0}C. Bottles were removed sequentially from the oven after the desired growth durations of 1, 3, 6, 9, and 12 hours. After the specific growth time at the desired temperature, the bottles were cooled down naturally to room temperature. Subsequently, the samples were taken out of the bottle and immediately rinsed thoroughly with de-ionized water to remove residual salt.

The nanorods were inspected using field emission scanning electron microscopy (FESEM). Preliminary composition check of the ZnO nanorods was done by Oxford made X-ray energy dispersive spectrometer (EDS) attached to the FESEM system. At least five different areas on each substrate were imaged to measure the nanorod density and to obtain the statistics on length and width values. High resolution transmission electron microscope (HRTEM), selected area electron diffraction (SAED), electron energy loss spectroscopy (EELS), and X-ray diffraction techniques were used to check crystal structure and growth orientation. The room temperature photoluminescence (PL) spectra were recorded using a FS920 Edinburgh unit using 325 nm, 15mW He-Cd laser as excitation source. The PL signal was collected using a single photon counting plug-in PC card with a resolution of 0.01 nm, and amplified by Hamamatsu R955 photomultiplier in a Peltier cooled housing. In all cases the twin nano wires were found uniformly spread over the entire substrate. Several PL scans from different parts of the same sample showed the same spectral features with only minor intensity variations.

Results and discussion

In a typical hydrothermal process, the precursor solution is allowed to react at a fixed reaction temperature (T_R), with the substrate immersed in the aqueous solution[22-24]. The resulting nanorods grow as uniform crystalline structures on the substrate.

A rather unexplored aspect of the hydrothermal process is the ability to form amorphous clusters of ZnO at temperatures below T_R, due to the lack of sufficient thermal energy for crystallization. For realizing ZnO nanorods in the CAC architecture, the amorphous region is desired at the middle of individual crystalline rods. For this purpose, unlike the standard practice, the substrates immersed in precursor solution were allowed to attain the final reaction temperature gradually from room temperature. During the initial stages of temperature ramping (below T_R) amorphous ZnO clusters grow at a slow rate until temperature reaches a minimum value of T_R. The minimum reaction temperature was found to be ~60 ^{0}C, for our experimental set-up. As the temperature reaches the minimum value of T_R, ZnO crystals start nucleating symmetrically from both sides of these amorphous clusters, ultimately providing the TNRJs in a CAC structure. The temperature ramp rate (R_r), therefore, determines the width of the amorphous layer in the TNRJs.
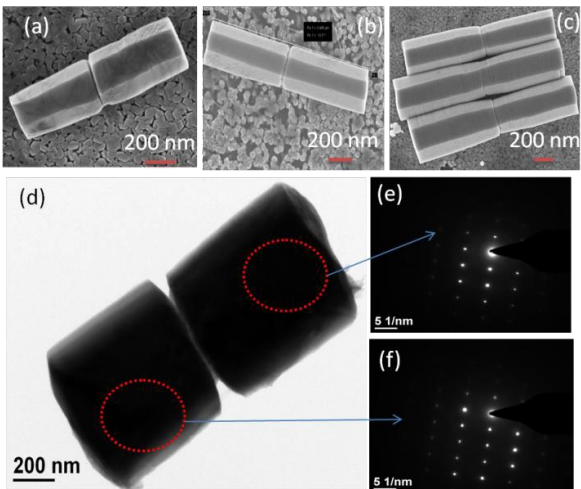

Fig. 1 (a), (b), and (c) show the scanning electron micrographs of ZnO nanorods prepared by this method at T_R = 60 ^{0}C (d) sample image of a single nanorod grown at a reaction temperature of 90 ^{0}C. The selected area diffraction patterns from both sides of the nanorods are shown in the panels (e) and (f).

Fig. 1 Panels (a), (b), and (c) show the scanning electron micrograph of twin nanorods prepared at a final reaction temperature of 60 ^{0}C, 80 ^{0}C, and 90 ^{0}C, respectively. Panel (d) shows a transmission electron
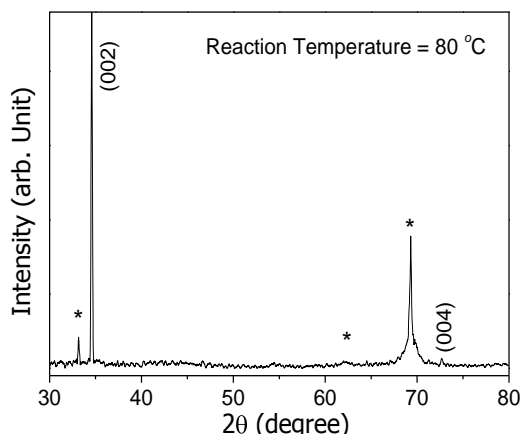

Fig. 2 Glancing angle (2^0) X-ray diffraction pattern of ZnO nanorods grown on Si substrates (*) at a reaction temperature of 80^{0}C. Only (00l) peaks are observed, owing to the highly oriented crystalline ZnO nanorods.

`a'), 80 $^0$C (sample `b') and 90 ^{0}C (sample `c'), respectively. In all cases the final reaction temperature was reached in 30 minutes, with effective ramp rates of ~1 ^{0}C/min, ~1.7 ^{0}C/min, and ~2 ^{0}C/min for samples a, b, and c, respectively. In all cases, hexagonal nanorods were obtained with a clear groove at mid length. Energy dispersive X-ray (EDX) analysis of the central grooved region did not show any signature of contamination, confirming continuous growth of ZnO crystals from amorphous ZnO. The dimensions of the nanorods were found to scale with the molar concentration of the precursor, T_R, and the reaction time, as expected. ZnO bipod structures have been reported earlier by Jang *et al.*[24], where acetate-intercalated zinc hydroxide double salt (Zn-HDS) was used as bi-directional nucleation seed for ZnO. This method, however, does not allow any control over the thickness of the interface between the two sides of the bipods, which is an essential feature for junction architecture. Figure 1(d) shows the transmission electron micrograph (TEM) of a nanorod prepared at 90 ^{0}C. Selected area electron diffraction (SAED) patterns on both sides of the central groove, shown in panels (e) and (f) in Fig. 1, confirm the crystalline nature of the [0001] grown nanorods. Grazing incidence X-ray diffraction measurements indicated (0001) oriented growth of the nanorods, as shown in Figure 2. Figure 3 (panels (a), (b), (c) , (e), and (f)) shows the scanning transmission electron microscopy (STEM)-energy dispersive x-ray (EDX) elemental map of a nanorod across the central groove. The line scan in panel (d) of Fig.3
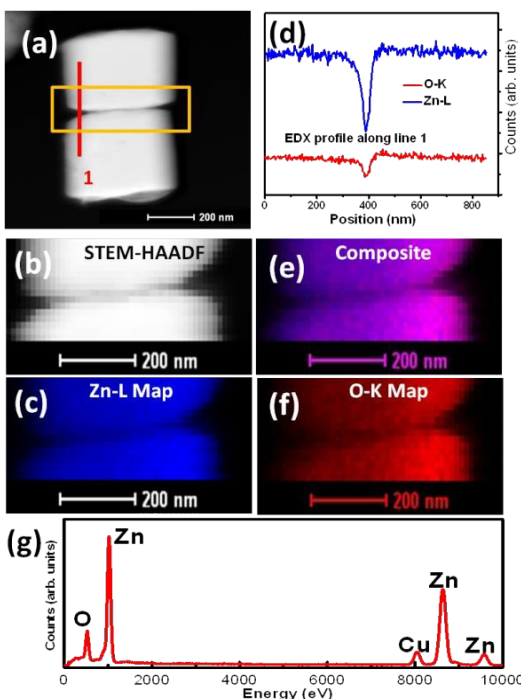
Fig. 3 Panel (a) shows the scanning transmission electron microscope image of a typical twin ZnO nanorod. Panel (b) shows the HAADF-STEM image for compositional sensitivity. Panels (c), (f) and (e) show elemental mapping for Zn, O and the composite image, respectively. Panel (f) shows the line scan across the junction. Panel (g) shows the STEM-EDX spectrum of the selected region in panel (a), confirming the presence of only Zn and O in the junction region. The Cu signal in this spectrum is from the Copper grid used in TEM imaging.

shows the Zn-L and O-K signals across the junction region. No signature of impurities was found in the amorphous region or along the body of the nanorod within the detection limit of STEM-EDX (0.1 at%). The EDX spectrum from the selected area of panel (a) is shown in panel (g) of Fig. 3. Apart from the Cu signal from the TEM grid, only Zn and O signals were detected confirming the absence of foreign elements. Figure 4 (a), and (f) show the high resolution TEM (HRTEM) image of the central grooved region of a nanorod grown at $T_R=60$ ^{0}C. The amorphous boundary between crystalline regions is apparent from these images. The fast Fourier transform (FFT) patterns, shown in panels (b), (c), and (d), of Fig. 4, also confirm the amorphous nature of the boundary. Fourier filtered images of the two crystalline lobes are presented in Fig. 4 (e) and (g). In Figure 5 (a), (b), and (c) we show the HRTEM images of the amorphous barrier regions of samples a, b, and c, respectively. Figure 5 (d)
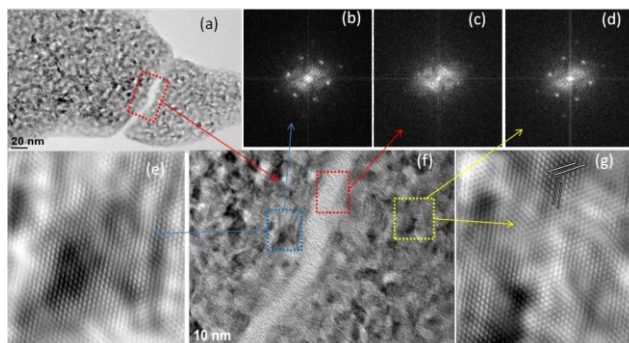

Fig. 4 Panel (a) shows the transmission electron image of the central region of a twin nanorod grown at a reaction temperature of 60 ^{0}C. The high resolution image of the amorphous gap is shown in the panel (f). Panels (b), (c) and (d) show the FFT patterns of the three indicates regions in panel (f). The magnified images of the crystalline segments on both sides of the amorphous gap are shown in panels (e) and (g).

shows the width of the amorphous barrier (d_a) calculated directly from the contrast of the amorphous layers in the TEM images. d_a was found to scale linearly with the duration, for which the precursor solution was allowed to remain below the minimum T_R, quantified by the temperature ramp rate R_r. The variation in the thickness of the amorphous layers at various spots is shown as the error bars. HRTEM shows that the interface between the crystalline and the amorphous portion is not atomically abrupt. However, such interfacial irregularities will be transparent to the optical phonon modes which have much longer wave length.
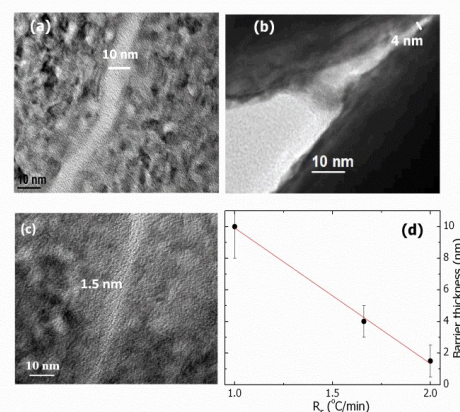

Fig. 5 Panels (a), (b), and (c) show the high resolution TEM images of the amorphous region at mid length of the twin nanorods. Panel (d) plots the average thickness of the amorphous layer as a function of the temperature ramp rate, as described in the text. The solid line is a fit showing linear scaling of the amorphous barrier thickness with temperature ramp rate.

Having established the formation of crystalline-amorphous-crystalline type TNRJs with controllable amorphous barrier we now discuss the suitability of these nanorods as effective phonon tunneling devices in which the barrier has low phonon transparency. For this purpose, we have utilized the characteristic phonon sidebands of free-exciton (FX) emission peaks, typically observed in PL spectra of wurtzite ZnO[34-36]. Such sideband emissions occur when free-excitons decay via emission of optical phonons. ZnO, being a polar semiconductor, experiences strong Frohlich interaction leading to frequent decay of free excitons via
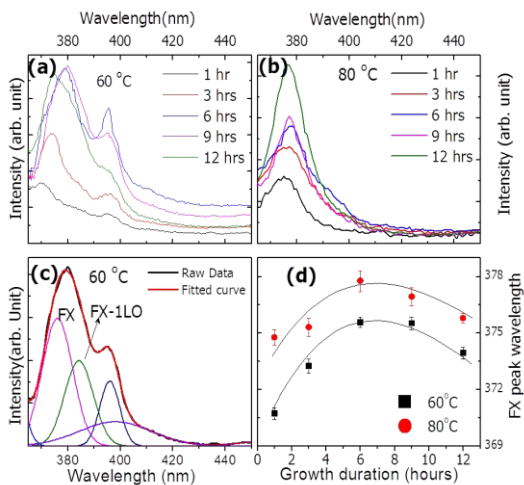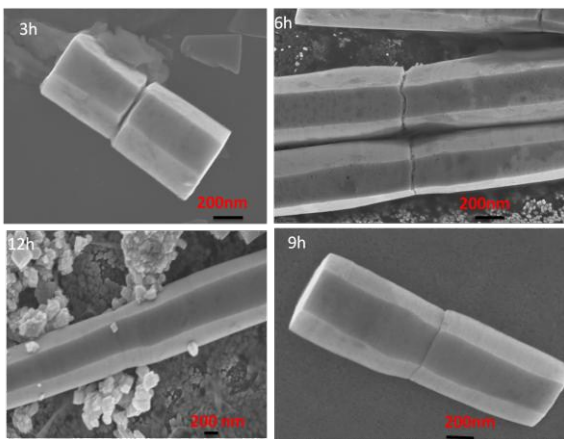

.

Figure 6 (a) and (b) show the room temperature PL spectra of TNRJs grown for 1, 3, 6, 9 and 12 hours with a molarity of 0.1M of each precursor at a reaction temperature of 60 ^{0}C and 80 ^{0}C, respectively. Strong UV emission peaks originating from near band edge (NBE) exciton decay are observed in all cases. Notice a significant asymmetry in the shape of the peaks, particularly for TNRJs grown at 60 ^{0}C, signifying the presence of convoluted phonon sidebands of the FX peaks. In addition, in Fig. 6(a) and (b) we notice that the peak positions shift as a function of growth duration. It is, however, misleading to discuss the peak shift without de-convoluting the free exciton peaks and the phonon side bands. Figure 6 (c) shows a sample de-convolution of PL spectrum of TNRJs grown at 60 ^{0}C for 9 hours. A commercial software (PeakFit) was used for the fitting purpose. The position of the FX peaks as a function of growth duration, extracted from the de-convolution procedure, has been plotted in the figure 6(d). For both 60 ^{0}C and 80 ^{0}C grown TNRJs an initial red shift of FX peak upto 6 hours was followed by a blue shift. Typically such shift in FX peak is believed to be a result of quantum confinement effects[37] or a manifestation of strain in the nanowires[35]. However, quantum confinement effects become relevant when the dimensions of the nanostructures become comparable to the free exciton Bohr radius (~ 3-4 nm) for ZnO[37].

Fig. 6 Panels (a) and (b) show the room temperature PL spectra of the twin nanorods for various growth durations at reaction temperatures 60 ^{0}C and 80 ^{0}C, respectively. Panel (c) shows a sample de-convolution of the measured PL spectrum indicating peaks corresponding to FX and FX-1LO emissions. The fitted curve is shown as the dotted line. Panel (d) plots the position of the FX peaks, extracted from de-convolution of the PL spectra in panels (a) and (b), as a function of the growth duration. The solid lines in panel (d) are only guides to the eye

one or more longitudinal optical (LO) phonon emission. The stacking of cations and aonions directly above each other, along the [0001] direction of wurtzite ZnO nanostructures, is particularly suitable for such LO phonon excitations. The characteristic energy of the lowest excited LO mode in ZnO is known[35,37] ~72 meV, leading to sidebands of FX emissions at ~72 meV intervals on the low energy side. The strong coupling of the FX and LO modes in ZnO provides an opportunity to establish the suitability of our TNRJs for more direct phonon tunneling experiments.
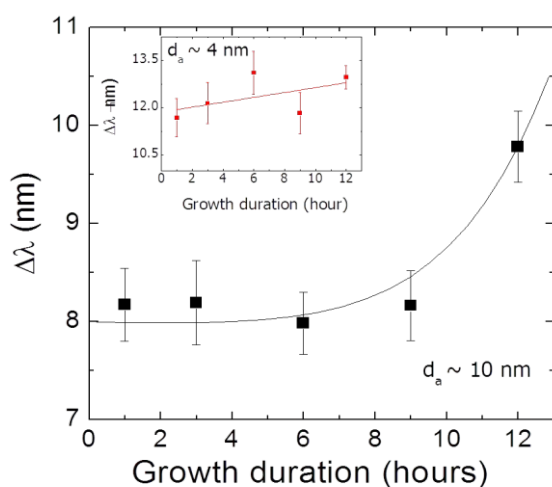
Fig. 8 The difference (Δλ) between the position of FX and FX-1LO peaks is plotted as a function of growth duration for nanorods with amorphous layer thickness $d_a \sim 10$ nm. The solid line is a guide to the eye. Inset shows the same plot for $d_a \sim 4$ nm. The solid line in the inset is a linear fit.

In our case, however, all relevant dimensions of the ZnO rods are orders of magnitude larger than the Bohr radius. Therefore, we have interpreted the shift in FX peak position as a signature of changing strain in the ZnO rods, consisted with previously reported[32] manifestation of tensile strain in ZnO nanowires. We note here that, as a function of growth duration, length and width of the nanorods were found to increase monotonously upto 12 hours. As the crystalline segments of TNRJs nucleate from the amorphous boundary at mid-length, the crystal structure is expected to be strained. Due to the low reaction temperature in the hydrothermal process, such strain keeps accumulating along the length of the rods. As a result, FX peak position shows a red shift upto 6 hour. Therefore, the blue shift after 6 hours, observed in Fig. 6(d), must be related to a relaxation of strain in the nanorods. In Figure 7 we show the electron micrographs of TNRJs grown at a fixed T_R of 60 ^{0}C for 3, 6, 9 and 12 hours. Notice that in the case of the 9 hours grown TNRJ, the amorphous gap appeared to fill up due to lateral growth of ZnO. For the 12 hours grown TNRJs (Fig 7(d)), two crystalline segments were completely bridged by ZnO, unlike the 3 hours grown TNRJs shown in Fig 7(a). We note here that, the lateral growth of crystalline ZnO only covers the amorphous region externally. The thickness of the amorphous layer, however, remains unchanged with growth duration. We believe that such bridging effectively relaxes the strain in both segments of the

TNRJs leading to the apparent blue shift in FX peak after 6 hours, observed in Fig 6(d).

As the FX peak shifts with strain in the system (which essentially scales with growth duration of TNRJs), the FX-1LO (first phonon side band) peak is also expected to shift by the same amount. Interestingly, however, we find a small, but measurable difference between the shift of the FX and the shift of the FX-1LO peaks for the TNRJs with ~10 nm amorphous barrier. We have plotted this difference between the positions of FX and FX-1LO peaks (defined as Δλ) as a function of growth duration, in Figure 8. A clear non-linearity is observed beyond 6 hours. The separation between the FX and the FX-1LO peaks (Δλ) essentially quantifies the energy transferred to the lattice (phonon mode) from the free exciton. Therefore, an increase in Δλ, as seen in Fig. 8, signifies an enhanced exciton-phonon interaction. The onset of the stronger FX-1LO interaction, in this case, shows a definitive correspondence with the onset of bridging of the amorphous gap in the TNRJs by lateral growth of ZnO beyond 6 hours, which effectively shorts the amorphous layer. We note that a similar bridging of the TNRJs also appears for the samples with ~ 4 nm amorphous barrier. Interestingly, however, no appreciable change in exciton-phonon interaction strength (equivalently, change in Δλ) was observed in this case due to the lateral bridging, as shown in the inset of Fig. 8. This result implies that while ~ 4 nm thick amorphous ZnO layer was transparent to the LO phonon modes, ~ 10 nm thick layer behaves as effective phonon barrier between the crystalline segments of the ZnO TNRJs.

Conclusions

In conclusion, using high resolution TEM we have shown that, nano scale junction engineering in a crystalline-amorphous-crystalline geometry is indeed possible by a single-step chemical process. Using de-convolution analysis of the phonon sidebands of free exciton emission peak in the PL spectrum we show that, beyond a certain thickness, the amorphous layers in the TNRJs work as effective phonon barriers. Although such nanoscale junction barriers will be transparent to long wavelength acoustic phonon modes, optical phonon mode excited on one crystalline side of the CAC junction is likely to get damped significantly at the amorphous barrier if the phonon mode wavelength is

comparable to the thickness of the barrier. Measuring the transmitted modal intensity of phonons on one crystalline side of the barrier by exciting phonon modes on the other crystalline side, using micro-Raman and atomic force microscopy based techniques, would provide a direct measure of the phonon tunneling co-efficient.

Acknowledgments

Notes and References

[1]School of Physical Sciences, National Institute of Science Education and Research (NISER) Bhubaneswar, Odisha, India-751005,0674-2304042, 2304028, E-mail: avanendra.s@niser.ac.in, pratap.sahoo@niser.ac.in, kartik@niser.ac.in

[2]Surface physics & Materials Science Division, Saha Institute of Nuclear Physics,1/AF Bidhannagar, Kolkata, India-700064 E-mail: biswarup.satpati@saha.ac.in

[3]Institute of Physics, Sachivalaya Marg, Bhubaneswar, Odisha, India-751005 E-mail: formohit@iopb.res.in

*Corresponding authors: pratap.sahoo@niser.ac.in, kartik@niser.ac.in

1. Z. T. Tian,B. E. White, Jr.,and Y. Sun *Appl. Phys. Lett.* 2010, **96**, 263113.
2. N. Yang; X. Xu; G. Zhang; B.,Li; *AIP Advances* 2012, **2**, 041410.
3. B. Li; J. Wang, *Phys. Rev. Lett.* 2003, **91**, 044301.
4. A. B. Djurišić; A. M. C. Ng; X. Y. Chen, *Prog. Quantum Electron.* 2010, **34**, 191-259.
5. M. Law; L. E. Greene; J. C. Johnson; R. Saykally; P. Yang, *Nat. Mater.* 2005, **4**, 455-459.
6. H. Kind; H. Yan; B. Messer; M. Law; P. Yang; *Adv. Mater.* 2002, **14**, 158-160.
7. M. H. Huang; S. Mao; H. Feick; H. Yan; Y. Wu; H. Kind; E. Weber; R. Russo; P. Yang; Y. I. Alivov; C. Liu; A. Teke; M. A. Reshchikov; S. Dogan; V. Avrutin; S.-J. Cho; H. Morkoc; *Science* 2001, **292**, 1897-1899.
8. D. M. Bagnall; Y. F. Chen; Z. Zhu; T. Yao; S. Koyama; M. Y. Shen; T. Goto, *Appl. Phys. Lett.* 1997, **70**, 2230-2232.
9. H. Tampo; P. Fons; A. Yamada; K.-K. Kim; H. Shibata; K. Matsubara; S. Niki; H. Yoshikawa; H. Kanie; *Appl. Phys. Lett.* 2005, **87**, 141904.
10. G. D. Cole; I. Wilson-Rae; K. Werbach; M. R. Vanner; M. Aspelmeyer, *Nat. Commun.* 2011, **2**, 231.
11. I. Wilson-Rae, *Phys. Rev. B* 2008, **77**, 245418.
12. Y. Gu; I. L. Kuskovsky; M. Yin; S. O'Brien; G. F. Neumark, *Appl. Phys. Lett.* 2004, **85**, 3833.
13. Ü, Özgür; Y. I. Alivov; C. Liu; A. Teke; M. A. Reshchikov; S. Dogan; V. Avrutin; S.-J. Cho; H. Morkoc, *J. Appl. Phys.* 2005, **98**, 041301.
14. C. X. Guo; Y. Dong; H. B. Yang; C. M. Li, Adv. Energy mater. 2013, **3**, 997-1003.
15. J. Xie; C. Guo; C. M. Li, Phys. Chem. Chem. Phys., 2013, 15, 15905-15911.
16. W. Hu; Z. Lu; Y. Liu; T. Chen; X. Zhou; C. M. Li; *Lab Chip*, 2013, 13, 1797-1802.
17. M. H. Huang; Y. Wu; H. Feick; N. Tran; E. Weber; P. Yang, *Adv. Mater.* 2001, **13**, 113-116.
18. W. Z. Xu; Z. Z. Ye; Y. J. Zeng; L. P. Zhu; B. H. Zhao; L. Jiang; J. G. Lu; H. P. He; S. B. Zhang, *Appl. Phys. Lett.* 2006, **88**, 173506.
19. L. Vayssieres; K. Keis; S.-E.; A.Hagfeldt, *J. Phys. Chem. B* 2001, **105**, 3350-3352.
20. L. Vayssieres, *Adv. Mater.* 2003, **15**, 464-466.
21. X. S. Nguyen; C. B. Tay; E. A. Fitzgerald; S. J. Chua, *Small* 2012, **8**, 1204-1208.
22. L. Schlur; A. Carton; P. Lévêque; D. Guillon; G. Pourroy, *J. Phys. Chem. C* 2013, **117**, 2993-3001.
23. J. J. Richardson; F. F. Lange, *Cryst. Growth Des.* 2009, **9**, 2576-2581.
24. W. Lin, D. Chen; J. Zhang; Z. Lin; J. Huang; W. Li; Y. Wang; F. Huang, *Crystal Growth & Design* 2009, **9**, 4378-4383.
25. Jang, E. S.; Won, J. H.; Hwang, S. J.; Choy, J. H. *Adv. Mater.* 2006, **18**, 3309-3312.
26. J. Schrier; D. O. Demchenko; L. W. Wang; A. P. Alivisatos, *Nano Lett.* 2007, **7**, 2377-2382.
27. M. Bitenc; G. Dražić; Z. C. Orel, *Cryst. Growth Des.* 2009, **10**, 830-837.
28. R. H. Wang; J. H. Xin; X. M. Tao, *Inorg. Chem.* 2005, **44**, 3926-3930.
29. E.-S. Jang; J.-H. Won; Y.-W. Kim; Z. Cheng; J.-H. Choy, *Cryst. Eng. Comm.* 2011, **13**, 546-552.
30. J. Zhan; Y. Bando; J. Hu; D. Golberg; K. Kurashima, *Small* 2006, **2**, 62-65.
31. H. Dong; Y. Yang; and G. Yang, *ACS Appl. Mater. Interfaces* 2014, **6**, 3093-3098.
32. F. Li; F Gong; Y. Xiao; A. Zhang; J. Zhao; S Fang.; D. Jia, *ACS Nano* 2013, **7**, 10482-10491.
33. M. Distaso; M. Mačković; E. Spiecker; W. Peukert, *Chemistry – A European Journal* 2014, **20**, 8199-8209.
34. T. Voss; C. Bekeny; L. Wischmeier; H. Gafsi; S. Borner; W. Schade; A. C Mofor.; A. Bakin; A. Waag, *Appl. Phys. Lett.* 2006, **89**, 182107.

35. B. Yan; R. Chen; W. Zhou; J. Zhang; H. Sun; H. Gong; T. Yu,
     Nanotechnology 2010, **21**, 445706.

36. W.-K. Hong; G. Jo; M. Choe; T. Lee; J. I. Sohn; M. E. Welland,
     Appl. Phys. Lett. **94**, 043103 (2009).

37. S. Y. Kim; Y. S. Yeon; S. M. Park; J. H. Kim; J. K. Song, Chem.
     Phys. Lett. 2008, **462** 100–103.